Full length article

The grain boundary stiffness and its impact on equilibrium shapes and boundary migration: Analysis of the Σ5, 7, 9, and 11 boundaries in Ni

Robert D. Moore[a], Timothy Beecroft[a], Gregory S. Rohrer[b], Christopher M. Barr[c],
Eric R. Homer[d], Khalid Hattar[c], Brad L. Boyce[c], Fadi Abdeljawad[a,e,*]

[a] Department of Mechanical Engineering, Clemson University, Clemson, South Carolina 29634, USA
[b] Department of Materials Science and Engineering, Carnegie Mellon University, Pittsburgh, Pennsylvania 15213, USA
[c] Sandia National Laboratories, Albuquerque, New Mexico 87185, USA
[d] Department of Mechanical Engineering, Brigham Young University, Provo, Utah 84602, USA
[e] Department of Materials Science and Engineering, Clemson University, Clemson, South Carolina 29634, USA

ARTICLE INFO

ABSTRACT

Grain boundaries (GBs) play a critical role in the formation of microstructure during materials processing and its subsequent evolution under service conditions. While GB misorientation is commonly used to describe the boundary's properties, a more complete description should also account for the GB plane normal, in which the GB stiffness is the relevant property controlling many GB dynamical processes. Herein, we leverage published atomistic simulation data to construct the full GB energy–plane normal diagrams for Σ5, 7, 9, and 11 GBs in Ni. The functional fits are used to obtain a complete mapping of the GB stiffness as a function of the plane normal, construct the equilibrium shapes, and determine the driving force for GB migration. It is shown that the GB stiffness can be larger in magnitude and more anisotropic than the energy itself. Further, many boundary inclinations are found to exhibit negative stiffness, indicating propensity for faceting. Results from our GB stiffness analysis are shown to be in qualitative agreement with experimental GB plane normal distributions in polycrystalline Ni. In broad terms, our results provide future avenues to account for the plane normal dependency of GB properties in mesoscale treatments of GB migration and microstructural evolution.

1. Introduction

Many problems in materials synthesis and processing can be cast as moving boundary problems [1]. An essential feature these problems have in common is the presence of materials interfaces, whose evolution over time greatly influences the formation and subsequent evolution of microstructure. Some prominent examples include crystal growth [2,3], sintering kinetics [4,5], precipitate coarsening [6], and electrodeposition [7]. In such problems, governing equations, typically in the form of differential equations, are derived to describe the dynamics of the materials system, and additional boundary conditions are prescribed on the moving interface in terms of the boundary's properties [8,9].

Of particular interest to many annealing treatments of polycrystalline metals is the migration of grain boundaries (GBs), as it controls the evolution of texture and grain size distribution and, as a result, the observable properties of these materials systems [10–12]. An accurate and predictive mesoscopic description of such processes requires as input several GB properties (e.g., energy and mobility) and their associated anisotropies. The GB geometry is characterized by eight degrees of freedom (DOF); five are termed macroscopic, and the other three are microscopic [13]. The microscopic DOF describe mutual translations of the two abutting grains making up the GB parallel and perpendicular to the GB plane. The five macroscopic DOF are divided into three describing the GB misorientation and two defining the GB plane normal **n**, or inclination [14,15].

Numerous studies have demonstrated the dependence of GB properties, such as energy [16], mobility [17] and self-diffusion [18], and other GB-related phenomena, including defect nucleation from [19,20] and defect interactions with GBs [21,22], on the GB geometric DOF. Theoretical [8,23–25] and computational [26–28] studies have shown that when considering the GB plane normal **n**, the interface stiffness, which not only depends on the GB free energy but also on its gradients with respect to **n**, is the thermodynamic property relevant to many GB dynamical

processes [29–31]. One such example that demonstrates the role of GB plane normal is the classic work of Hsieh and Balluffi [30], in which GBs with prescribed misorientation DOF were shown to transform *from a structure with a single plane normal to one made of two facets, each with a well defined plane normal*, analogous to a single phase transforming to two phases. Because of this analogy, these distinct GB states are referred to as GB phases. Cahn provided a detailed thermodynamic analysis of GB phases and possible types of phase transitions, including ones driven by the GB plane normal DOF [32].

While GB properties and associated anisotropies have been the subject of active research, detailed calculations and analysis of the GB stiffness have been limited. From a computational point of view, determination of the GB stiffness requires a knowledge of not only the energy at the inclination of interest, but also higher order energy gradients with respect to **n**. As a result, a complete mapping of GB energy is needed, which requires free energy calculations at a prescribed temperature for many inclinations. This step has limited the determination of the GB stiffness, as it requires a substantial computational effort. To the best of our knowledge, only two studies, one employing the capillary fluctuation method [33] and the other using curvature-driven flow of well-controlled geometries [34], have been used to calculate the stiffness of specific GB inclinations. *Schratt* et al. [35] *employed quasi-equilibrium grain shapes from atomistic simulations to calculate the inclination dependency of the interface energy for several GBs.* Very recently, Abdeljawad et al. [36] provided a complete mapping, or a tensorial description, of the GB stiffness as a function of the plane normal DOF for $\Sigma 3$ GBs.

The goal of this study is to provide theoretical analysis and analytical calculations of the GB stiffness and its role in GB migration. To this end, we leverage recent high throughput atomistic calculations of GB energy in Ni to construct and obtain analytical fits of the GB energy-plane normal diagram. The fits are then used to calculate the GB stiffness as a function of the complete plane normal DOF and the resultant GB equilibrium shapes. As a demonstration, the interface stiffness is calculated for the $\Sigma 5, 7, 9$, and 11 GBs in Ni. The rest of the manuscript is organized as follows: Theory and analysis are presented in Section 2, where Section 2.1 presents the theoretical aspects of the GB stiffness and Section 2.2 presents the application to several GBs in Ni. The results and discussion are presented in Section 3. Finally, Section 4 provides concluding remarks and summary of the work.

2. Theory and analysis

2.1. The interface stiffness tensor

We first begin with a two-dimensional (2D) demonstration in order to highlight the role of GB stiffness. Figure 1(a) depicts two configurations of a GB, where the first is a system with a flat GB profile at its local equilibrium and the second is one with an inclined GB that makes an angle θ with respect to the initial GB profile. With this geometry, the misorientation DOF are fixed and the GB free energy can be parametrized as $\gamma(\mathbf{n}) = \gamma(\theta)$. Following the treatment of Cabrera [37] and Privman [38], it is shown in Appendix A that the energy change $\Delta\gamma$ as the GB changes its profile from the one in configuration 1 to that in configuration 2 is given by

$$\Delta\gamma = \frac{1}{2}(\gamma + \gamma_{\theta\theta})\theta^2 + \cdots, \tag{1}$$

where $\gamma_{\theta\theta} = \partial^2\gamma/\partial\theta^2$ and γ is measured in the reference state, i.e., configuration 1. It can be seen from Eq. 1 that the magnitude of the GB stiffness, $\gamma + \gamma_{\theta\theta}$, controls the energy change and its sign provides a measure of interface stability. If $\gamma + \gamma_{\theta\theta} > 0$, then

any distortion in the GB profile increases the energy. On the other hand, $\gamma + \gamma_{\theta\theta} < 0$ leads to an unstable equilibrium case, where distortions in the GB profile lead to a decrease in the energy.

We now shift our attention to three-dimensional geometries, where the GB is in general a curved surface. In their non-equilibrium thermo-mechanics treatment of problems involving moving boundaries with anisotropic properties, Gurtin et al. [8,24,25,39] arrived at sharp interface equations involving the interface stiffness tensor $\Gamma(\mathbf{n})$ given by

$$\Gamma(\mathbf{n}) = \gamma\mathbf{I} + \nabla_{\mathbf{n}}\nabla_{\mathbf{n}}\gamma \tag{2}$$

where again γ is the interface free energy, $\mathbf{I}$ is the identity tensor and $\nabla_{\mathbf{n}}$ is the surface gradient with respect to $\mathbf{n}$ on the surface of a unit sphere in $\mathbb{R}^3$. Using the spherical coordinate system [refer to Fig. 1(b)], the GB plane normal $\mathbf{n}$ can be parametrized using the polar θ and azimuthal ϕ angles such that $\Gamma(\mathbf{n}) = \Gamma(\theta, \phi)$. With this parametrization, diagonalization of Γ leads to the following for the principal values, or eigenvalues, (λ_1, λ_2) of the GB stiffness tensor for gently varying GB energy profiles [36]

$$\lambda_1 = \gamma + \gamma_{\theta\theta} \tag{3a}$$

$$\lambda_2 = \gamma + \gamma_{\phi\phi} \tag{3b}$$

where again $\gamma_{\theta\theta} = \partial^2\gamma/\partial\theta^2$ and $\gamma_{\phi\phi} = \partial^2\gamma/\partial\phi^2$. As noted above, the stiffness reduces to $\gamma + \gamma_{\theta\theta}$ in 2D systems. *It can be seen from Eqs. (2) and (3) that for the interface stiffness to be defined, the interface energy has to be twice differentiable with respect to the spherical angles. Cusps in the interface energy-inclination profile represented by an analytical function will therefore require regularization. For example, in problems involving faceted solidification Debierre* et al. [40] *introduced smooth functions around cusps in the solid-liquid interface energy-inclination diagram.*

Several geometrical means to characterizing the plane normal dependency of the interfacial energy and resultant equilibrium shapes have been proposed and used, including the classic Wulff construction [41], Herring tangent spheres [42,43], inverse-γ diagrams [42], and Cahn and Hoffman's ξ-capillarity vector [44,45]. With the tangent sphere approach, the equilibrium shape is constructed from the locus of sphere centers passing through the origin, touching the γ surface and lying within it. The inverse-γ diagram is a polar diagram of the reciprocal of the interface free energy, i.e., the $\{\mathbf{n}\gamma^{-1}\}$ plot. The ξ-capillarity vector is defined by [44,45]

$$\xi \equiv \nabla[r\gamma(\theta, \phi)] = \gamma\hat{\mathbf{e}}_r + \gamma_{\theta}\hat{\mathbf{e}}_{\theta} + \frac{1}{\sin\theta}\gamma_{\phi}\hat{\mathbf{e}}_{\phi} \tag{4}$$

where $\hat{\mathbf{e}}_r$, $\hat{\mathbf{e}}_{\theta}$, and $\hat{\mathbf{e}}_{\phi}$ are the unit vectors along the radial, polar, and azimuthal directions, respectively and the ∇ operator is expressed in spherical coordinates. Boundary inclinations with negative interface stiffness values, or so-called forbidden orientations [46,47], correspond to non-convex regions of $\{\mathbf{n}\gamma^{-1}\}$ [42] or ears (i.e., multivaluedness) in the ξ-vector [28,48,49].

Several interfacial instabilities arise due to negative interface stiffness [43,50,51]. A flat interface will spontaneously break up into facets, or hill-and-valley structures, with facet junctions/corners connecting them if its initial inclination is not part of the Wulff equilibrium shape. Cabrera [37] examined interface energy-inclination diagrams and showed that faceting is an interface structural transition, similar to phase separation in immiscible bulk systems. Angenent and Gurtin [24] investigated the structural stability of moving boundaries and classified them as strictly stable, stable, or unstable according to $\gamma + \gamma_{\theta\theta} > 0$, $\gamma + \gamma_{\theta\theta} \geq 0$, and $\gamma + \gamma_{\theta\theta} < 0$. Several studies examined the evolution of interfaces with highly anisotropic properties and even ones
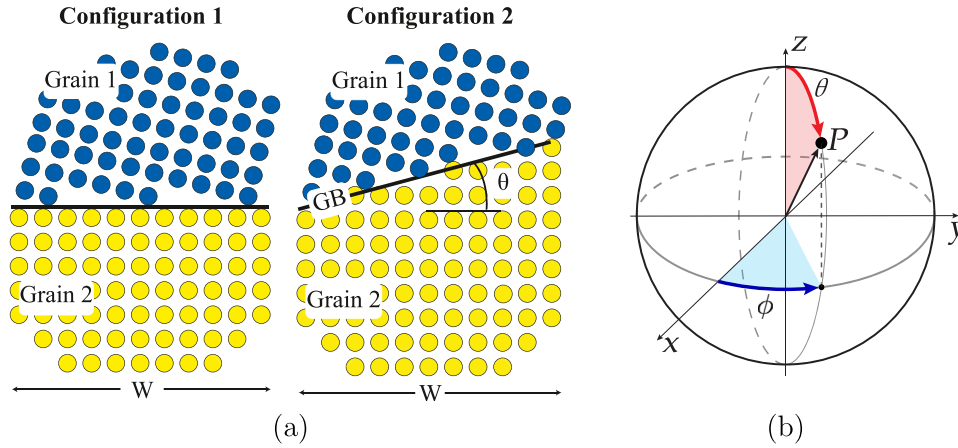
Fig. 1. (a) A configuration of a GB plane at a reference inclination (left) and one that is inclined by an angle θ (right). (b) The spherical coordinate system used in this work, where θ and ϕ denote the polar and azimuthal angles, respectively.
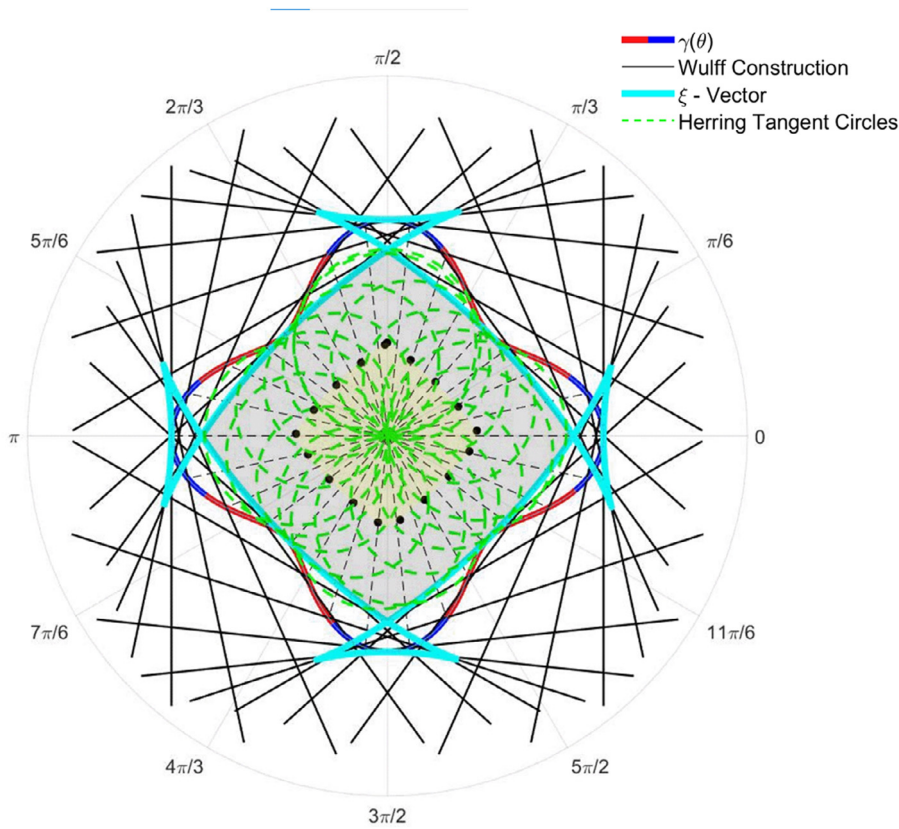
Fig. 2. An animation depicting the various vector thermodynamic treatments of the plane normal dependency of the interface free energy. For this 2D demonstration, $\gamma(\theta) = 1 + 0.2\cos(4\theta)$. The GB energy is colored by the stiffness, where red (blue) denotes positive (negative) stiffness. *For the online version, please embed the movie directly within the text. For the print version, please include the movie in supplemental materials and add link to it in the text (For interpretation of the references to color in this figure legend, the reader is referred to the web version of this article.).*

exhibiting negative stiffness values for some range of inclinations [26,28,29,40,47,49,52–55]. Video 2 shows an animation illustrating the above-mentioned vector thermodynamic techniques assuming an interface energy of the form $\gamma = 1 + \epsilon\cos(4\theta)$, where $\epsilon = 0.2$ (notice $\epsilon > 1/15$ leads to negative stiffness).

We now shift our attention to GB dynamics. Assuming isothermal conditions with no bulk driving forces, Gurtin's treatment [8,39] yields the following for the GB normal velocity

$$\mathcal{V}_n = M_{gb}\boldsymbol{\Gamma}(\mathbf{n}) : \mathbf{K} = M_{gb}[\gamma\mathcal{K} + (\nabla_\mathbf{n}\nabla_\mathbf{n}\gamma) : \mathbf{K}] \qquad (5)$$

where M_{gb} is the GB mobility, $\mathbf{K} = -\nabla_s\mathbf{n}$ is the curvature tensor of the interface s [8], $\mathbf{A}:\mathbf{B}$ is the usual tensor double dot product, and $\mathcal{K} = \mathrm{tr}(\mathbf{K})$ is the trace of the curvature tensor (i.e., twice the mean curvature) [8]. In 2D systems, this treatment reduces to a kinetic law of GB migration described by $\mathcal{V}_n = M_{gb}(\gamma + \gamma_{\theta\theta})\mathcal{K}$ [23,50,56]. Further, under the isotropy assumption, Eq. (5) reduces to $\mathcal{V}_n = M_{gb}\gamma\mathcal{K}$ corresponding to the widely used kinetic law for GB migration [57]. In cases where the eigenvectors of the stiffness and curvature tensors align, $\boldsymbol{\Gamma} : \mathbf{K} = \lambda_1\kappa_1 + \lambda_2\kappa_2$, where (κ_1, κ_2) corresponds to the principal curvatures and, as a

result, Eq. 5 above reduces to

$$\mathcal{V}_n = M_{gb}\big[(\gamma + \gamma_{\theta\theta})\kappa_1 + (\gamma + \gamma_{\phi\phi})\kappa_2\big]. \tag{6}$$

On the other hand, when the eigenvectors of the stiffness and curvature tensors do not align, then the stiffness tensor should be transformed in accordance with tensor transformation laws [27]. However, for the remainder of this study, the principal stiffness values $\lambda_1 = \gamma + \gamma_{\theta\theta}$ and $\lambda_2 = \gamma + \gamma_{\phi\phi}$ will be used to examine GB stability and driving force for migration, as these represent the largest and smallest possible values of the interface stiffness. A close examination of Eq. (6) above shows that the GB stiffness affects GB migration in two main ways. First, the GB stiffness deviates in magnitude and degree of anisotropy from the interface energy. For example, in solidification problems several studies on solid-liquid interfaces have shown that the interface stiffness is much more anisotropic than the interface energy itself [3,58]. The second role deals with the sign of GB stiffness, where in 2D $\gamma + \gamma_{\theta\theta} < 0$ indicates a structural instability of the interface with respect to faceting [24]. In general, non-faceted GBs are rough and are thought to move without a barrier to reduce curvature [59]. If a faceted interface includes a singular orientation, it moves to reduce the weighted mean curvature and there might be a nucleation energy barrier to migration [59,60].

2.2. Application to GBs in Ni

In this section, the principal stiffness values λ_1 and λ_2 of several GBs in Ni will be used to elucidate deviations of the GB stiffness from the GB energy in terms of both magnitude and degree of anisotropy, and how such deviations impact the driving force for GB migration.

Our approach in calculating the principal stiffness values is as follows: First, we leverage recent high throughput published atomistic data of GB energy in Ni to map out the GB energy-plane normal surface, where again the boundary normal is parametrized by the polar θ and azimuthal ϕ spherical angles. Olmsted et al. [16,17] performed atomistic simulations of bicrystals to calculate the 0 K GB energy in Ni, and their calculations showed excellent agreement with experimentally obtained GB energies [61]. In this work, the published GB energy data of Olmsted [16] for the $\Sigma 5, 7, 9$, and 11 GBs, where $1/\Sigma$ represents the ratio of lattice points that are in coincidence (i.e., the coincidence site lattice description [13]), will be used. Second, with the aid of the fundamental zone concept in systems exhibiting multiplicity of rotations [62], the atomistic data will be used to map the full energy-plane normal space. Based on the treatment of Patala and Schuh [63], Homer et al. [64] constructed a set of regions in plane normal space in which indistinguishable rotations are represented only once. Finally, twice-differentiable basis functions of the spherical angles θ and ϕ will be used to fit the atomistic GB energy data, which will then be used in the stiffness calculations. It is worth noting that while several options for basis function sets are available to expand the energy surface $\gamma(\mathbf{n})$, computational efficiency is considered here, as such functional fits serve as key input parameters in several mesoscale models of microstructural evolution, such as phase field [65,66], front tracking [67], and Potts [66,68]. In addition to the goodness of the energy fits, the number of function evaluations and their computational tractability are considered. In this work, least square fitting using real-valued 2D Fourier series [refer to Appendix B] is employed to fit the atomistic data.

2.3. Published experimental observations

Our theoretical analysis and analytical calculations will be compared with experimentally determined GB plane distributions

(GBPDs), which quantify the relative areas of GB planes as function of the GB five macroscopic DOF. We will use the GBPDs of Ni measured by Randle et al. [69] and focus specifically on the distribution of GB planes at the $\Sigma 5, 7, 9$ and 11 misorientations. This data is available from the GB Data Archive [70]. The data used here was derived from Ni in a reference state, before GB engineering, as described by Randle et al. [69]. *Electron backscatter diffraction (EBSD) with a step size of $\sim 2\ \mu m$ was used to map the shapes and orientations of more than 20,000 grains. Individual areas of 1-4 mm^2 were recorded for a total mapped area of $\sim 120\ mm^2$. From the orientation maps, more than 8.3×10^5 GB traces were measured. Here, it is worth noting that due to the spatial resolution of EBSD, nanoscale faceted GBs and their plane normals were not resolved and only the average plane normal across any nanoscale facets was reported.* The GBPD was then calculated from these data using an established stereological procedure [71]. The GBPD at each misorientation includes boundaries within $\pm 5°$ of the ideal orientation. The relative areas of GB planes are given in units of multiples of a random distribution (MRD); 1 MRD is equivalent to the area expected in a random, isotropic distribution and values greater (less) than unity correspond to orientations with more (less) area than expected in a random distribution.

3. Results and discussion

We begin by obtaining functional fits for the GB energy $\gamma(\theta, \phi)$ for $\Sigma 5, 7, 9$, and 11 GBs in Ni using the atomistic data by Olmsted et al. [16]. *Using the convention in Fig. 1(b), the polar and azimuthal angles are respectively measured from: [100] and $[0\bar{1}3]$ for $\Sigma 5$; [111] and $[4\bar{5}1]$ for $\Sigma 7$; [110] and $[1\bar{1}4]$ for $\Sigma 9$; and [110] and $[1\bar{1}3]$ for $\Sigma 11$ GBs.* Our functional fits [refer to Appendix B] for the energy surface of these GBs are given by

$$
\begin{aligned}
\gamma_{\Sigma 5}(\theta, \phi) =\ & \alpha_0 + \alpha_1 \sin(\theta) + \alpha_2 \sin(3\theta) + \alpha_3 \cos(4\phi) \\
& + \alpha_4 \cos(8\phi) + \alpha_5 \sin(\theta)\cos(4\phi) + \alpha_6 \sin(\theta)\cos(8\phi) \\
& + \alpha_7 \sin(3\theta)\cos(4\phi) + \alpha_8 \sin(3\theta)\cos(8\phi),
\end{aligned} \tag{7a}
$$

$$
\begin{aligned}
\gamma_{\Sigma 7}(\theta, \phi) =\ & \alpha_0 + \alpha_1 \sin(\theta) + \alpha_2 \cos(3\phi) + \alpha_3 \cos(6\phi) \\
& + \alpha_4 \sin(\theta)\cos(3\phi) + \alpha_5 \sin(\theta)\cos(6\phi),
\end{aligned} \tag{7b}
$$

$$
\begin{aligned}
\gamma_{\Sigma 9}(\theta, \phi) =\ & \alpha_0 + \alpha_1 \sin(\theta) + \alpha_2 \cos(2\theta) + \alpha_3 \cos(4\theta) \\
& + \alpha_4 \cos(2\phi) + \alpha_5 \sin(\theta)\cos(2\phi) \\
& + \alpha_6 \cos(2\theta)\cos(2\phi) + \alpha_7 \cos(4\theta)\cos(2\phi),
\end{aligned} \tag{7c}
$$

$$
\begin{aligned}
\gamma_{\Sigma 11}(\theta, \phi) =\ & \alpha_0 + \alpha_1 \sin(\theta) + \alpha_2 \cos(4\theta) + \alpha_3 \cos(2\phi) \\
& + \alpha_4 \cos(4\phi) + \alpha_5 \sin(\theta)\cos(2\phi) \\
& + \alpha_6 \sin(\theta)\cos(4\phi) + \alpha_7 \cos(4\theta)\cos(2\phi) \\
& + \alpha_8 \cos(4\theta)\cos(4\phi),
\end{aligned} \tag{7d}
$$

where $\gamma_{\Sigma 5}, \gamma_{\Sigma 7}, \gamma_{\Sigma 9}$, and $\gamma_{\Sigma 11}$ denote the energy functions for $\Sigma 5, 7, 9$, and 11 GBs, respectively. Here, $\{\alpha_i : i = 0, \cdots, 8\}$ are the fitting coefficients, whose values are listed in Table 1. The function fits in Eq. (7) result in R^2 values of 0.9809, 0.9949, 0.9147, and 0.9775 for $\Sigma 5, 7, 9$, and 11 GBs, respectively. *Here, we note that Eq. (7) incorporates the symmetries of these GBs [63] and, as a result, the structure of the fits holds for all FCC metals. However, the magnitude of the fitting coefficients will depend on the material type and temperature. Holm et al. [72] showed that the energy of many GB types in several FCC metals is scaled by the metal's shear modulus.* Plots of the GB energy surface using the fits in Eq. (7) are shown in Fig. 3 for $\Sigma 5$ [Fig. 3(a)], $\Sigma 7$ [Fig. 3(b)], $\Sigma 9$ [Fig. 3(c)], and $\Sigma 11$ [Fig. 3(d)] GBs. *As discussed above, the symmetries used*

Table 1
Values of the fitting parameters $\{\alpha_i : i = 0, \ldots, 8\}$ in Eq. (7) that are used to fit the atomistic energy data for $\Sigma 5, 7, 9,$ and 11 GBs in Ni.
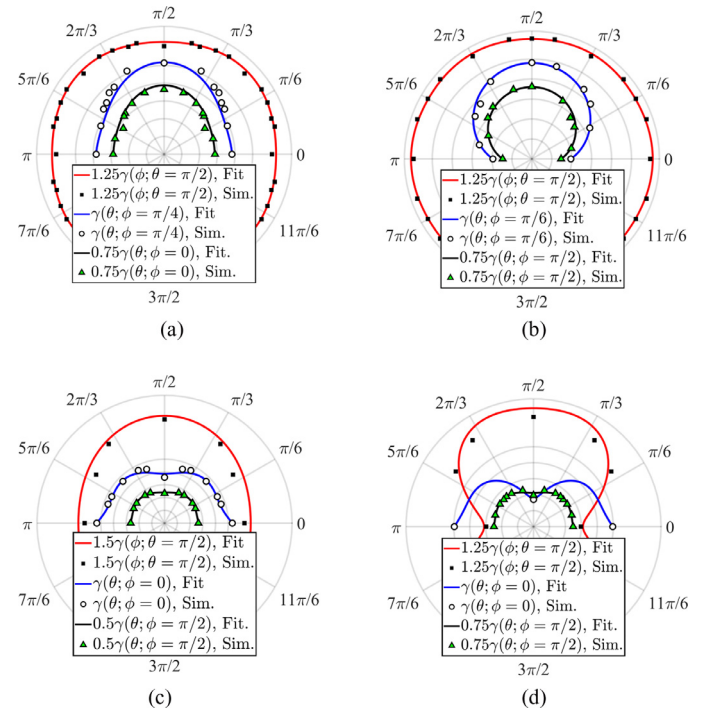
GB Energy Fitting Parameters [10^{-3} Jm^{-2}]								
Σ	α_0	α_1	α_2	α_3	α_4	α_5	α_6	α_7	α_8
5	956.5	244.4	-93.34	3.376	-3.254	-45.89	11.98	-13.45	9.354
7	490.8	715.9	-0.3512	3.104	0.4101	2.936	—	—	—
9	1639	-671.9	-212.8	-97.31	175.1	-415.4	-148.6	-25.67	—
11	1346	-399.4	-104.2	38.43	16.13	-308.0	-91.75	-38.37	-16.05
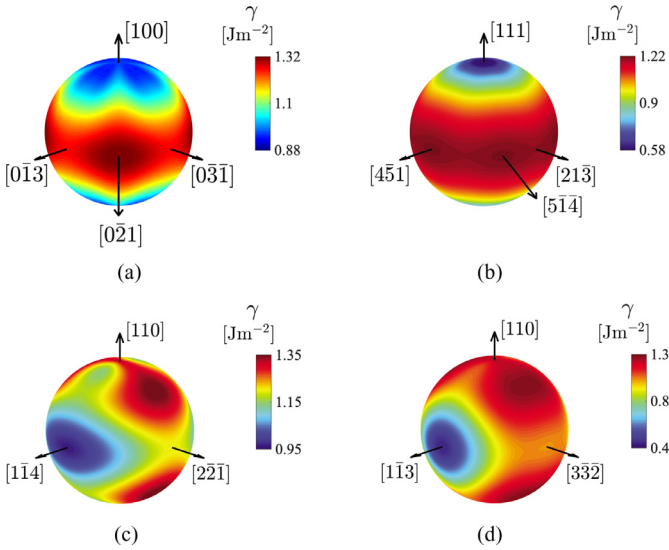
Fig. 3. The GB energy as a function of the plane normal **n** for (a) $\Sigma 5$, (b) $\Sigma 7$, (c) $\Sigma 9$, and (d) $\Sigma 11$ GBs. Here, $\mathbf{n} = \mathbf{n}(\theta, \phi)$, refer to Fig. 1(b) for the spherical angle convention used in this work. *The polar and azimuthal angles are respectively measured from:* [100] *and* [01̄3] *for* $\Sigma 5$; [111] *and* [45̄1] *for* $\Sigma 7$; [110] *and* [11̄4] *for* $\Sigma 9$; *and* [110] *and* [11̄3] *for* $\Sigma 11$ *GBs.*

Fig. 4. Representative slices from the GB energy surfaces shown in Fig. 3 for (a) $\Sigma 5$, (b) $\Sigma 7$, (c) $\Sigma 9$, and (d) $\Sigma 11$ GBs in Ni. The plots show the atomistic simulation data (markers) from the study by Olmsted et al. [16] and the fits (solid lines) using Eq. (7).

to construct $\gamma(\theta, \phi)$ for each GB followed the approach by Patala and Schuh [63] and Appendix B provides a description of the process of expanding γ using Fourier series of θ and γ. The reader is referred to the Supplementary Material Section for the Matlab R2019a [73] scripts used to generate the plots in Fig. 3. Again, the reference polar and azimuthal axes for each GB are respectively: [100], [01̄3] for $\Sigma 5$; [111], [45̄1] for $\Sigma 7$; [110], [11̄4] for $\Sigma 9$; and [110], [11̄3] for $\Sigma 11$ GBs. For each GB energy plot, the polar z-axis is chosen to align with the misorientation axis, which makes the reference axis for the azimuthal angle a symmetric tilt GB orientation. Further, at the polar angle $\theta = \pi/2$, the azimuthal angle ϕ traces out the zone of tilt GBs. Variations in the GB energy by up to $\approx 50\%, 200\%, 50\%, 300\%$ for $\Sigma 5, 7, 9,$ and 11 GBs, respectively, can be observed as a function of GB plane normal. For the $\Sigma 5$ and 7 GBs, the energy is a weakly varying function of the azimuthal angle [cf. Fig. 3(a) and (b)]; however, a more pronounced dependency on the azimuthal angle can be seen for $\Sigma 9$ and 11 GBs. Further, low-energy GBs with plane normals of $\langle 100 \rangle$, $\langle 111 \rangle$, $\langle 114 \rangle$, and $\langle 113 \rangle$, corresponding to $\Sigma 5, 7, 9,$ and 11 GBs, respectively, can be seen.

To demonstrate the goodness of our GB energy fits, representative slices of the GB energy surface $\gamma(\theta, \phi)$ are shown in Fig. 4 for $\Sigma 5$ [Fig. 4(a)], $\Sigma 7$ [Fig. 4(b)], $\Sigma 9$ [Fig. 4(c)], and $\Sigma 11$ [Fig. 4(d)] GBs. The markers correspond to the atomistic data points from the study by Olmsted et al. [16] and the solid lines are the energy fits using Eq. (7). In all panels of Fig. 4, the solid red lines correspond to the slice $\theta = \pi/2$, describing energy variations along the azimuthal direction. For the $\Sigma 5$ GB, the azimuthal slices $\phi = 0, \pi/4$ are shown in Fig. 4(a) as these exhibit the largest energy vari-

ations along the polar directions. For the $\Sigma 7$ GB, the azimuthal slices $\phi = \pi/6, \pi/2$ are shown in Fig. 4(b), while the azimuthal slices $\phi = 0, \pi/2$, describing the largest variations along the polar directions are shown in Fig. 4(c) and (d) for the $\Sigma 9$ and 11 GBs, respectively. The low-energy $\Sigma 11\{113\}$ GB can be seen in Fig. 4(d). It can be clearly seen that the functional forms in Eq. (7) provide an excellent fit to the atomistic data.

Next, the functional fits in Eq. (7) are used to calculate the principal GB stiffness values $\lambda_1 = \gamma + \gamma_{\theta\theta}$ and $\lambda_2 = \gamma + \gamma_{\phi\phi}$ describing the driving force for GB migration, and the results are shown in Figs. 5, 7, 9, 11 for $\Sigma 5, 7, 9,$ and 11 GBs, respectively. Based on the energy fits in Eq. (7), the spatial gradients of the GB energy are functions of θ and ϕ and, as a result, the principal stiffness values λ_1 and λ_2 are also functions of both θ and ϕ.

We first start with the $\Sigma 5$ GB, where Fig. 5 shows the GB stiffness results. Fig. 5(a) depicts a surface plot of $\lambda_1 = \gamma + \gamma_{\theta\theta}$, where it can be seen that a wide range of GB plane normals that are coplanar with the $\langle 013 \rangle$ and $\langle 021 \rangle$ directions are characterized by small and some are negative $\gamma + \gamma_{\theta\theta}$ stiffness values. Similarly, Fig. 5(b) is a surface plot of $\gamma + \gamma_{\phi\phi}$, where it can also be seen that several GB inclinations have negative $\gamma + \gamma_{\phi\phi}$ stiffness values. As discussed above, inclinations with negative stiffness values are forbidden ones and will be missing from the equilibrium shape. Further, it can be seen that the stiffness values are more
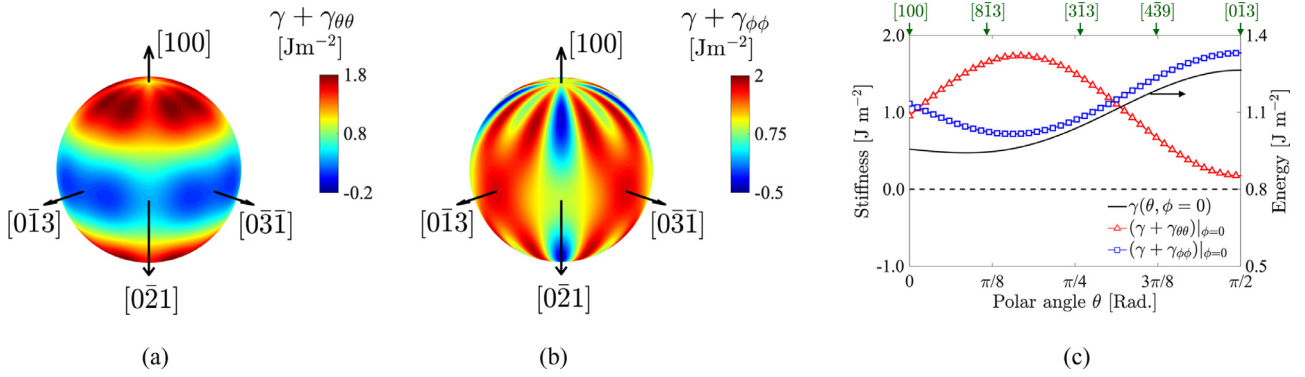
Fig. 5. For the Σ5 GB in Ni, principal stiffness values (a) $\gamma + \gamma_{\theta\theta}$ and (b) $\gamma + \gamma_{\phi\phi}$. (c) A line scan along $\phi = 0$ depicting the polar angle dependency of the GB energy and principal stiffness values.
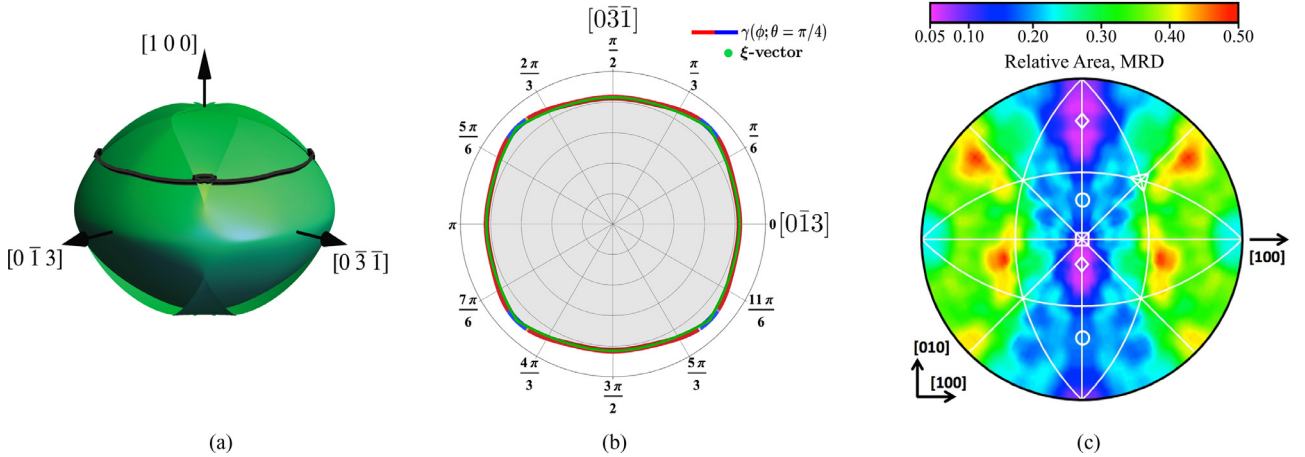
Fig. 6. For the Σ5 GB in Ni, (a) a plot of the Cahn-Hoffman ξ-vector using the functional form of $\gamma(\theta, \phi)$ given by Eq. (7). (b) A slice along $\theta = \pi/4$ depicting the ξ-vector (green) and GB energy colored by the $\gamma + \gamma_{\phi\phi}$ stiffness, where red (blue) denote positive (negative) values. (c) Experimentally-determined relative areas of GB planes, shown in stereographic projection along the [001] direction. The orientation of the [100] misorientation axis is shown by the arrow. The white square (triangle) denotes the [001] ([111]) directions. The white diamonds mark the orientations of the $(031)||(0\bar{3}1)$ and $(0\bar{1}3)||(0\bar{1}\bar{3})$ symmetric tilt GBs, and the white circles mark the orientations of the $(012)||(0\bar{2}\bar{1})$ and $(0\bar{2}1)||(01\bar{2})$ symmetric tilt GBs (For interpretation of the references to color in this figure legend, the reader is referred to the web version of this article.).

anisotropic functions than the GB energy itself [refer to Fig. 3(a)]. To demonstrate this effect, Fig. 5(c) shows a line scan along $\phi = 0$ (i.e., plane spanned by $[0\bar{1}3]$ and [100]), depicting the polar angle dependency of the energy, $\gamma + \gamma_{\theta\theta}$, and $\gamma + \gamma_{\phi\phi}$. Along this line scan, the GB energy changes by $\sim 25\%$, whereas the stiffness values vary by more than $\sim 100\%$.

We now use Cahn-Hoffman ξ-capillarity vector to examine the equilibrium shape of the Σ5 GB. The reader is referred to the Supplementary Material Section for the Mathematica v11 [74] notebooks used to generate the ξ-vector plots in Figs. 6(a), 8(a), 10(a), and 12(a). Fig. 6(a) shows a plot of the ξ-vector, where ears can be observed over some range of GB plane normals, indicating structural instability and the propensity of these GB inclinations to break up into facets. As a demonstration, Fig. 6(b) shows a slice along $\theta = \pi/4$ [black line in Fig. 6 (a)] depicting both the ξ-vector in green and the GB energy colored by the $\gamma + \gamma_{\phi\phi}$ stiffness, where red (blue) denote positive (negative) stiffness values. The shaded region in gray corresponds to the equilibrium shape. Along this slice, there exists a range of GB normals (e.g., ϕ in the range of $\pi/6$ and $\pi/3$) with negative $\gamma + \gamma_{\phi\phi}$ stiffness, and such inclinations are missing from the equilibrium shape given by the shaded region in gray. Next, we compare our analytical interface stiffness results with the experimentally-obtained GBPD. Fig. 6(c) depicts the GBPD distribution obtained by Randle et al. [69] for Σ5 GBs in Ni shown in stereographic projection along the [001] direction. The white diamonds mark the orientations of the $(031)||(0\bar{3}1)$
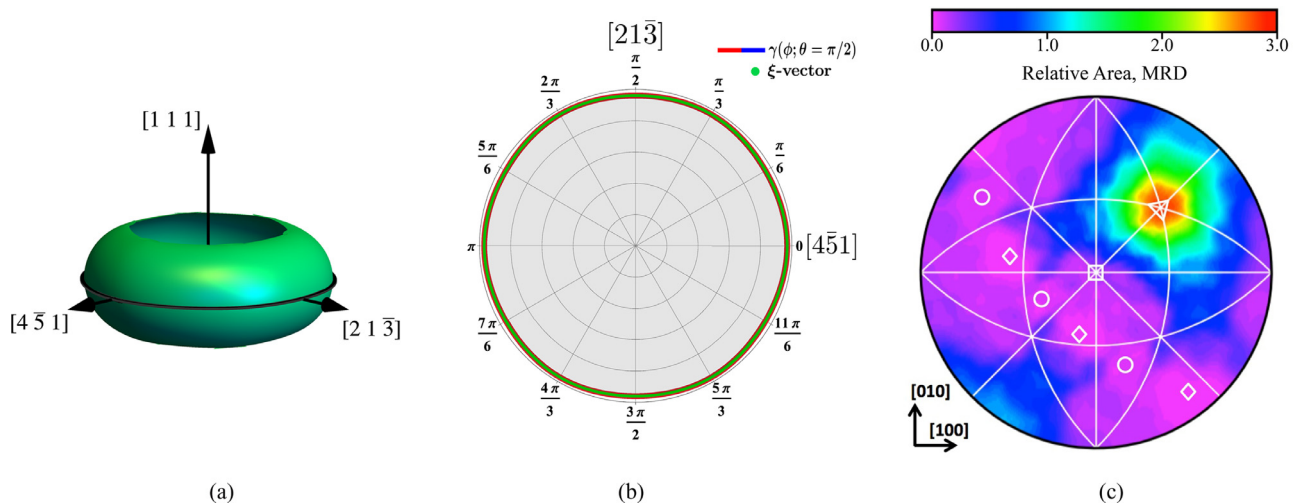
and $(0\bar{1}3)||(0\bar{1}\bar{3})$ symmetric tilt GBs, and the white circles mark the orientations of the $(012)||(0\bar{2}\bar{1})$ and $(0\bar{2}1)||(01\bar{2})$ symmetric tilt GBs. Fig. 5(a) shows that GBs with normals in the vicinity of $\langle 013 \rangle$ and $\langle 021 \rangle$ have slightly negative stiffness values and, thus, are structurally unstable [24] and, which in turn explains the low observed relative area for these inclinations. Indeed, all GB inclinations that are coplanar with $\langle 013 \rangle$ and $\langle 021 \rangle$ have the smallest relative area, which is consistent with our stiffness results in Fig. 5(a).

Next, we examine Σ7 GBs, where the stiffness results are shown in Fig. 7. The $\gamma + \gamma_{\theta\theta}$ stiffness map is depicted in Fig. 7(a), where it can be seen that variations in the $\gamma + \gamma_{\theta\theta}$ stiffness are small and are in the range of 0.47–0.5 Jm^{-2}. Fig. 7(b) shows the $\gamma + \gamma_{\phi\phi}$ stiffness, where large variations, in the range of 0.4–1.4 Jm^{-2}, can be seen. Fig. 7(c) shows a representative line scan along the polar angle for $\phi = 0$ (i.e., plane spanned by the $\langle 111 \rangle$ and $\langle 4\bar{5}1 \rangle$), depicting constant $\gamma + \gamma_{\theta\theta}$ stiffness values. Further, $\gamma + \gamma_{\phi\phi}$ values are larger in magnitude than $\gamma + \gamma_{\theta\theta}$ leading to a larger driving force for GB migration [cf. Eq. (6)] along the azimuthal direction. For this Σ7 GB, the principal stiffness values are found to be positive for all values of θ and ϕ, indicating that all inclinations of the Σ7 may appear in the equilibrium shape.

We now turn our attention to the equilibrium shape of the Σ7 GB. Fig. 8(a) depicts the ξ-vector for the Σ7 GB, where no ears in the shape appear due to the positive stiffness values for all θ and ϕ. As an example, Fig. 8(b) shows a line scan along the $\theta = \pi/2$ [black line in Fig. 8(a)] depicting both the ξ-vector in green and
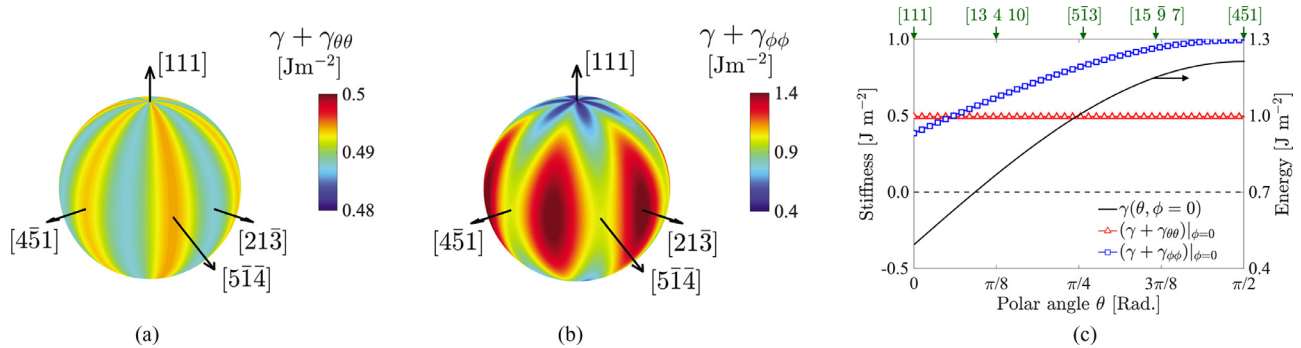
Fig. 7. For the Σ7 GB in Ni, principal stiffness values (a) $\gamma + \gamma_{\theta\theta}$ and (b) $\gamma + \gamma_{\phi\phi}$. (c) A line scan along $\phi = 0$ depicting the polar angle dependency of the GB energy and principal stiffness values.
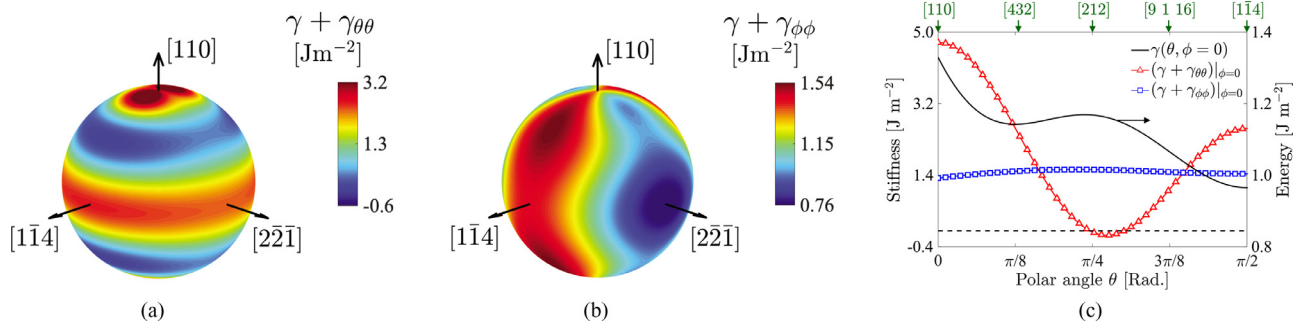

Fig. 8. For the Σ7 GB in Ni, (a) a plot of the Cahn-Hoffman ξ−vector. (b) A line scan along $\theta = \pi/2$ depicting the ξ−vector (green) and GB energy, which is colored by the stiffness $\gamma + \gamma_{\phi\phi}$, where red (blue) denote positive (negative) stiffness values. (c) Experimentally-determined relative areas of GB planes, shown in stereographic projection along the [001] direction. The direction of the misorientation axis, [111], is denoted by the white triangle, and the [001] direction is at the position of the white square. The three white circles mark the orientations (left to right) of the $(\bar{3}21)||(2\bar{3}1)$, $(\bar{2}\bar{1}3)||(3\bar{1}2)$, and $(1\bar{2}3)||(12\bar{3})$ symmetric tilt GB, and the three white diamonds mark the orientations (left to right) of the $(\bar{5}14)||(5\bar{4}\bar{1})$, $(\bar{1}45)||(41\bar{5})$, and $(4\bar{5}1)||(\bar{1}5\bar{4})$ tilt GBs (For interpretation of the references to color in this figure legend, the reader is referred to the web version of this article.).

the GB energy colored by the $\gamma + \gamma_{\phi\phi}$ stiffness, where red denotes positive GB stiffness values. Along this line, all plane normals of this GB appear in the equilibrium shape, which is given by the shaded region in gray. The Σ7 GB exhibits a low-energy inclination along $\langle 111 \rangle$ [cf. Fig. 3(b)] and this is also evident in the ξ-vector plot. The experimentally-obtained GBPD by Randle et al. [69] is shown in Fig. 8(c), which depicts the GBPD distribution shown in stereographic projection along the [001] direction. The direction of the misorientation axis, [111], is denoted by the white triangle, and the [001] direction is at the position of the white square. The three white circles mark the orientations (left to right) of the $(\bar{3}21)||(2\bar{3}1)$, $(\bar{2}\bar{1}3)||(3\bar{1}2)$, and $(1\bar{2}3)||(12\bar{3})$ symmetric tilt GBs, and the three white diamonds mark the orientations (left to right) of the $(\bar{5}14)||(5\bar{4}\bar{1})$, $(\bar{1}45)||(41\bar{5})$, and $(4\bar{5}1)||(\bar{1}5\bar{4})$ tilt GBs. The experimental GBPD shows similar, yet low observed relative areas for the (451) and (213), which is consistent with the results in Fig. 8(b) depicting a near circular equilibrium shape along the $\theta = \pi/2$ slice containing these inclinations. The experimental GBPD shows a maximum in the relative area for the Σ7(111) twist GB, which is also consistent with the ξ-plot in Fig. 8(a).
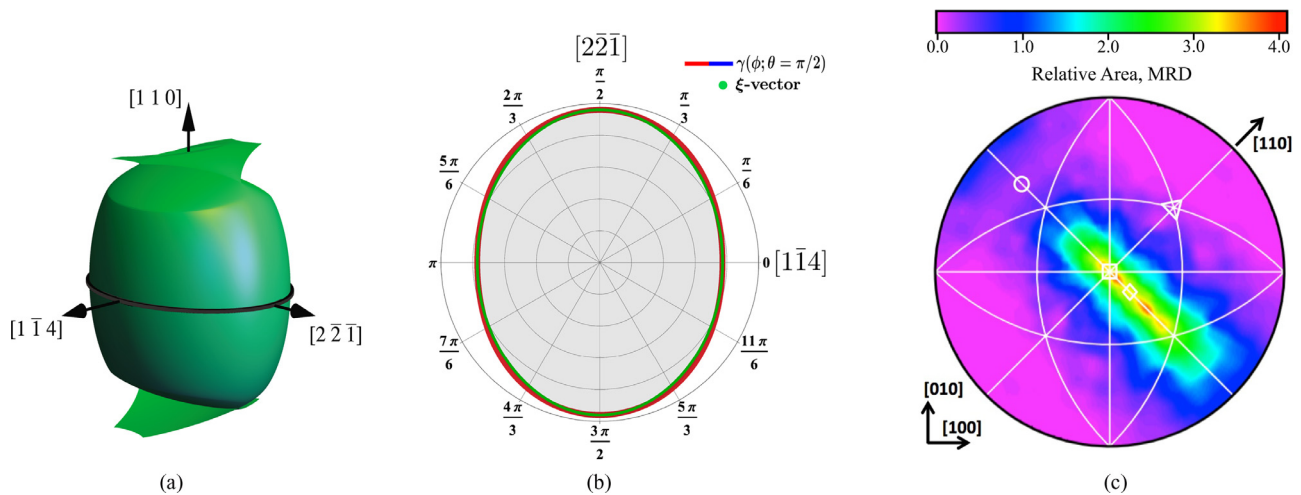
The next GB we consider is the Σ9 GB, where Fig. 9 depicts the stiffness results. Fig. 9(a) is a surface plot of $\gamma + \gamma_{\theta\theta}$, which shows large variations in the stiffness values. Further, $\gamma + \gamma_{\theta\theta}$ attains negative values over some range of inclinations (e.g., in the neighborhood of $(\theta, \phi) \sim (\pi/4, 0)$). The surface plot of $\gamma + \gamma_{\phi\phi}$ is shown in Fig. 9(b), where it can be seen that the stiffness values

exhibit larger variations than the energy itself [refer to Fig. 3(c)]. Also, $\gamma + \gamma_{\phi\phi}$ is positive for all values of θ and ϕ. Fig. 9(c) shows a representative line scan along $\phi = 0$, depicting the energy, $\gamma + \gamma_{\theta\theta}$, $\gamma + \gamma_{\phi\phi}$ values. Along this line, $\gamma + \gamma_{\theta\theta}$ exhibits larger variations than the energy itself. The results depicted in Fig. 9 demonstrate the complexity of the driving force for GB migration when the complete plane normal DOF are accounted for. For example, for this Σ9 GB the driving force for GB migration [cf. Eq. (6)] along the polar direction exhibits a larger magnitude and higher degree of anisotropy than the one along the azimuthal direction.

Next, Fig. 10(a) shows a plot of the ξ-vector for the Σ9 GB, where ears (i.e., self intersecting segments) appear in the ξ-plot corresponding to regions with negative $\gamma + \gamma_{\theta\theta}$ stiffness in Fig. 9(a). This in turn results in a faceted ξ-plot, as inclinations with negative stiffness will be missing from the equilibrium shape. Along the azimuthal direction, however, stiffness values are all positive. For example, Fig. 10(b) shows a slice along $\theta = \pi/2$, which represents the plane spanned by the $\langle 114 \rangle$ and $\langle 221 \rangle$, depicting the ξ-vector in green and GB energy, which is colored by the stiffness $\gamma + \gamma_{\phi\phi}$, where red (blue) denote positive (negative) stiffness values. It can be seen that along this slice the stiffness is positive and all inclinations are part of the equilibrium shape. Fig. 10(a) and (b) shows that the equilibrium shape of the Σ9 GB in Ni is an ellipsoidal cylinder with faceted caps. The experimentally-obtained GBPD by Randle et al. [69] is shown in Fig. 10(c), which depicts the GBPD distribution shown in stereographic projection along the

Fig. 9. For the Σ9 GB in Ni, principal stiffness values (a) $\gamma + \gamma_{\theta\theta}$ and (b) $\gamma + \gamma_{\phi\phi}$. (c) A line scan along $\phi = 0$ depicting the polar angle dependency of the GB energy and principal stiffness values.

Fig. 10. For the Σ9 GB in Ni, (a) a plot of the Cahn-Hoffman $\xi-$vector. (b) A line scan along $\theta = \pi/2$ depicting the $\xi-$vector (green) and GB energy, which is colored by the stiffness $\gamma + \gamma_{\phi\phi}$, where red (blue) denote positive (negative) stiffness values. (c) Experimentally-determined relative areas of GB planes, shown in stereographic projection along the [001] direction. The orientation of the [110] misorientation axis is shown by the arrow, and the [001] direction is at the position of the white square. The [111] direction is denoted by the white triangle. The white diamond and circle mark, respectively, the orientation of the $(1\bar{1}4)||(1\bar{1}\bar{4})$ and $(\bar{2}21)||(2\bar{2}\bar{1})$ symmetric tilt GBs (For interpretation of the references to color in this figure legend, the reader is referred to the web version of this article.).

[001] direction. The orientation of the [110] misorientation axis is shown by the arrow, and the [001] direction is at the position of the white square at the center of the plot. The [111] direction is denoted by the white triangle. A diffuse region of large relative areas can be seen around the white diamond, which marks the $(1\bar{1}4)||(1\bar{1}\bar{4})$ symmetric tilt GB. This is consistent with the ξ-vector plot in Fig. 10(a), where $\langle 114 \rangle$ and plane normals in its vicinity form the sides of the ellipsoidal cylinder that makes up the equilibrium shape of this GB. Further, the white circle marks the orientation of the $(\bar{2}21)||(2\bar{2}\bar{1})$ symmetric tilt GB, which is characterized by small relative areas. The Σ9(221) GB corresponds to the vertices of the ellipsoidal cuts of the equilibrium shape depicted in Fig. 10(b), which cover less area than its sides, i.e., (114) orientations. It is also worth noting that the relatively high population of Σ9 GBs is a consequence of the large concentration of Σ3 boundaries. Whenever two Σ3 GBs meet at a triple line, the third boundary must be a Σ9 [75].

The final boundary of interest is the Σ11 GB. Fig. 11(a) and (b) shows the $\gamma + \gamma_{\theta\theta}$ and $\gamma + \gamma_{\phi\phi}$ stiffness plots, respectively, where it can be seen that both attain negative values over some range of inclinations. Further, variations in both $\gamma + \gamma_{\theta\theta}$ and $\gamma + \gamma_{\phi\phi}$ are found to be greater than the energy itself, which is in the range of 0.4–1.3 Jm^{-2} [refer to Fig. 3(d)]. As an example, Fig. 11(c) shows a line scan along $\phi = 0$ (i.e., plane spanned by the $\langle 110 \rangle$ and $\langle 113 \rangle$) depicting the energy, $\gamma + \gamma_{\theta\theta}$, and $\gamma + \gamma_{\phi\phi}$ values. Again, negative $\gamma + \gamma_{\theta\theta}$ values in the polar angle range of $\theta \in [\pi/8, 3\pi/8]$ can be seen indicating that these will be missing from the equilibrium shape. Also, the Σ11(113) is a very low-energy GB compared to the

other Σ11 inclinations, which explains the large positive stiffness value of this inclination, i.e., any perturbation in the boundary profile about this inclination causes a large increase in the energy of the system.

Next, a plot of the ξ-vector for the Σ11 GB is shown Fig. 12(a), where ears, i.e., self-intersecting regions, can be seen over some range of inclinations. For example, Fig. 12(b) depicts a slice along $\theta = \pi/2$ (i.e., plane spanned by the $\langle 113 \rangle$ and $\langle 332 \rangle$), showing the ξ-vector in green and GB energy colored by the stiffness $\gamma + \gamma_{\phi\phi}$, where red (blue) denote positive (negative) stiffness. The missing inclinations within this slice are ones exhibiting negative stiffness (i.e., segments of the energy curve that are colored in blue). It can be seen from Fig. 12(a) and (b) that the equilibrium shape of the Σ11 GB is a rectangular prism with curved faces and sharp edges and is mainly composed of planes with normals that are centered around the $\langle 113 \rangle$ and $\langle 332 \rangle$ directions, with the $\langle 113 \rangle$ being the dominant one, refer for Fig. 12(a). The experimentally-obtained GBPD for the Σ11 GB is shown in Fig. 12(c), which depicts relative areas of GB planes, shown in stereographic projection along the [001] direction. The orientation of the [110] misorientation axis is shown by the arrow, and the [001] direction is at the position of the white square. The [111] direction is denoted by the white triangle. The white diamond and circle mark, respectively, the orientation of the $(1\bar{1}3)||(1\bar{1}\bar{3})$ and $(\bar{3}32)||(3\bar{3}\bar{2})$ symmetric tilt GBs. A diffuse peak in the relative areas can be seen around the $\langle 113 \rangle$ direction (i.e., white diamond in Fig. 12(c)), indicating that this is a frequently observed inclination for the Σ11 GB. Further, small relative areas are observed for (332) GBs, which is consistent with the
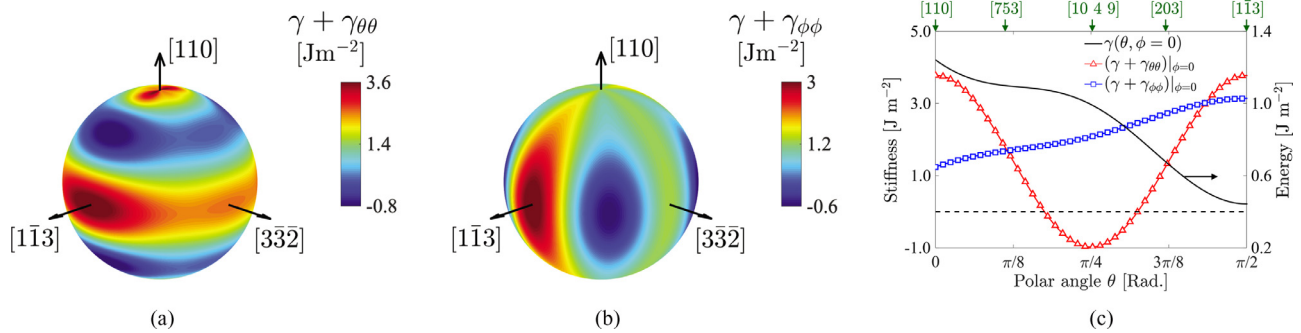
Fig. 11. For the $\Sigma 11$ GB in Ni, principal stiffness values (a) $\gamma + \gamma_{\theta\theta}$ and (b) $\gamma + \gamma_{\phi\phi}$. (c) A line scan along $\phi = 0$ depicting the polar angle dependency of the GB energy and principal stiffness values.
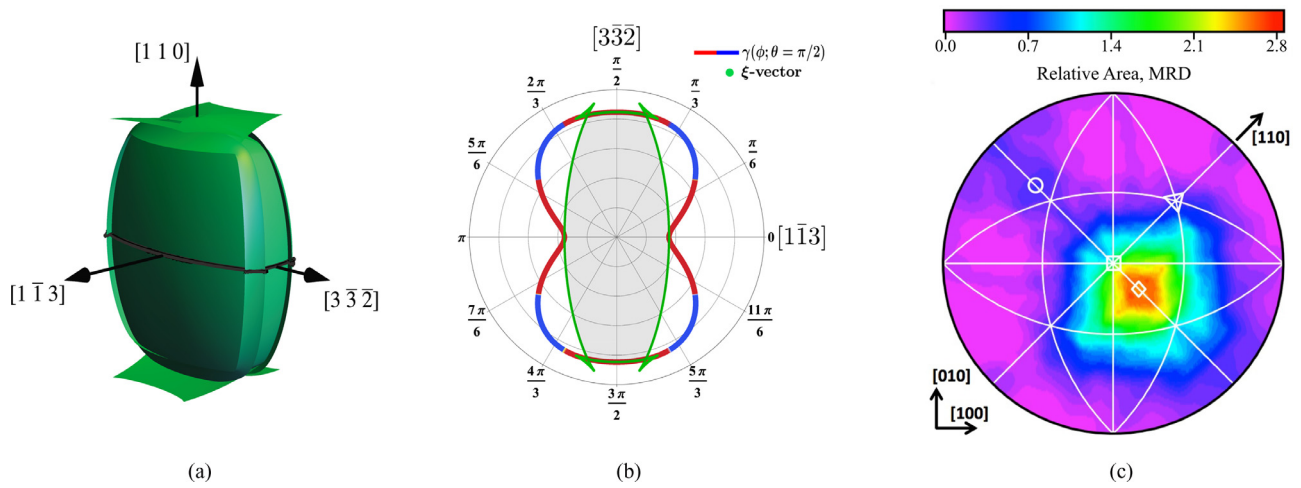
Fig. 12. For the $\Sigma 11$ GB in Ni, (a) a plot of the Cahn-Hoffman $\xi-$vector. (b) A line scan along $\theta = \pi/2$ depicting the $\xi-$vector (green) and GB energy, which is colored by the stiffness $\gamma + \gamma_{\phi\phi}$, where red (blue) denote positive (negative) stiffness values. (c) Experimentally-determined relative areas of GB planes, shown in stereographic projection along the [001] direction. The orientation of the [110] misorientation axis is shown by the arrow, and the [001] direction is at the position of the white square. The [111] direction is denoted by the white triangle. The white diamond and circle mark, respectively, the orientation of the $(1\bar{1}3)||(1\bar{1}\bar{3})$ and $(\bar{3}32)||(3\bar{3}\bar{2})$ symmetric tilt GBs (For interpretation of the references to color in this figure legend, the reader is referred to the web version of this article.).

ξ-vector plot showing an equilibrium shape that is composed of large (small) areas of (113) ((332)) orientations.

Our results demonstrate that when considering the GB plane normal DOF, the GB stiffness is the relevant property describing the driving force for curvature-driven GB migration. Further, it is shown that the GB principal stiffness values exhibit drastically different magnitudes and degree of anisotropy than the GB energy itself. This has several important implications for GB migration. First, a negative stiffness indicates a forbidden, or missing, orientation from the equilibrium shape, and it will not be observed experimentally. The stiffness results shown in this work are consistent with the experimentally-observed GBPDs for Ni. Second, if one of the missing GB inclinations forms through highly non-equilibrium processing techniques or during grain growth, then this inclination has to re-orient to one on the Wulff shape, or break up into facets, whose length scales might be beyond the resolution of EBSD measurements. This indicates that the GB network plays a role, as it may impart geometric constraints that force certain GBs to curve, or bow, thus changing their plane normal. This in turn changes the boundary's stiffness and, as a result, the driving force for GB migration.

It is also worth mentioning that our stiffness results represent the athermal limit; it employs atomistic GB energies at 0 K. However, the anisotropy in GB energy and consequently the GB stiffness were found to decrease with increasing temperature [34,76]. Therefore, one may regard our athermal limit for the GB stiffness as the extreme case for anisotropies based on plane normal DOF. Also, our results indicate that the GB stiffness for each GB

misorientation, described in this work by the Σ value, has a different functional form in terms of the spherical angles θ and ϕ. This in turn highlights the need to account for such anisotropies in mesoscale models, which typically use the same functional form for the plane normal dependency across all GB misorientations [77,78]. Finally, while our results are focused on Ni mainly due to the availability of complete GB energy–plane normal data and experimental GBPDs, the approach highlighted in this work is materials agnostic—it is applicable to a wide range of metallic systems if their GB energy-plane normal diagrams are available.

4. Summary and Conclusion

Grain boundaries and associated anisotropy in their properties play a critical role in microstructure formation and evolution during materials processing or under service conditions. When considering the GB plane normal DOF, the GB stiffness is the relevant thermodynamic property that influences the driving force for GB migration. However, GB stiffness data are very limited in the literature due to the substantial computational effort associated with calculating the GB free energy as a function of plane normal. In this work, we used atomistic data for the energy of $\Sigma 5$, 7, 9, and 11 GBs in Ni at 0 K to map out the GB energy-plane normal diagrams and obtain analytical fits in terms of the spherical angles, i.e., $\mathbf{n} = \mathbf{n}(\theta, \phi)$. The energy functions for these GBs were then used to obtain a complete mapping of the GB principal stiffness values, and the results were compared with experimentally-obtained GB plane normal distributions in Ni.

It was found that for a wide range of inclinations the GB stiffness is larger in magnitude and more anisotropic than the GB energy itself. The stiffness for the $\Sigma7$ GB was found to exhibit the weakest anisotropy, whereas the stiffness for the $\Sigma9$ and 11 GBs showed largest variations and strongest anisotropy compared to their respective energies. Further, negative stiffness values were found for a range of inclinations indicating structural instabilities with respect to faceting with some $\Sigma9$ and 11 GB inclinations exhibiting the most negative stiffness values. All stiffness values for the $\Sigma7$ were found to be positive indicating that all inclinations of this GB appear in the equilibrium shape. Our analysis of the $\Sigma5$, 7, 9, and 11 GBs in Ni demonstrates that the GB stiffness greatly influences the driving force for GB migration. In broad terms, our work provides an avenue to account for the plane normal DOF in mesoscopic treatments of texture and microstructural evolution of polycrystalline systems.

Declaration of Competing Interest

Acknowledgment

Appendix A. The interface stiffness: 2D case

For a 2D system, Fig. 1(a) depicts two configurations of a GB, where the first is a system with a flat GB profile at its local equilibrium and the second is an inclined GB that makes an angle θ with respect to the initial GB profile. In both configurations, the misorientation DOF are held fixed. The free energy in both configurations is given by:

$$G_1 = G_b + \gamma(\theta_o)A_o, \tag{A.1}$$

$$G_2 = G_b + \gamma(\theta)A, \tag{A.2}$$

where G_b is the bulk free energy, which we assume it does not change. θ_o and A_o are defined in configuration 1, whereas $\gamma(\theta)$ and A are defined in configuration 2. We require $\Delta G = G_2 - G_1 \le 0$ leading to

$$\Delta G = \gamma(\theta)A - \gamma(\theta_o)A_o \le 0. \tag{A.3}$$
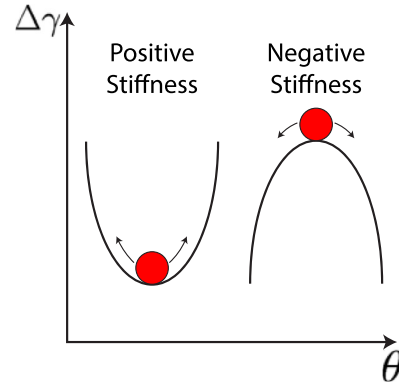

Fig. A.13. A schematic illustration of Eq. (A.6). The stiffness corresponds to the local curvature of the $\Delta\gamma - \theta$ diagram.

Next, we divide throughout by A_o and define $\Delta\gamma$ as

$$\Delta\gamma = \frac{\Delta G}{A_o} = \frac{\gamma(\theta)A}{A_o} - \gamma(\theta_o) \le 0, \tag{A.4}$$

where the term $\gamma(\theta)A/A_o$ is coined the projected interfacial energy [37,38]. According to Fig. 1, $A = A_o/\cos(\theta)$, which leads to

$$\frac{\gamma(\theta)A}{A_o} = \frac{\gamma(\theta)}{\cos(\theta)} = \left(\gamma_o + \gamma_\theta\theta + \frac{1}{2}\gamma_{\theta\theta}\theta^2 + \cdots\right)\left(1 + \frac{1}{2}\theta^2 + \cdots\right), \tag{A.5}$$

where with no loss of generality Taylor expansion of $\gamma(\theta)$ and $1/\cos(\theta)$ about $\theta = 0$ is used. $\gamma_o = \gamma(0)$, $\gamma_\theta = (\partial\gamma/\partial\theta)_{\theta=0}$, and $\gamma_{\theta\theta} = (\partial^2\gamma/\partial\theta^2)_{\theta=0}$. Upon expanding the terms on the right hand side of Eq. (A.5) and inserting the result in Eq. (A.4), one arrives at the following for $\Delta\gamma$

$$\Delta\gamma = \frac{1}{2}(\gamma_o + \gamma_{\theta\theta})\theta^2 + \cdots \tag{A.6}$$

Here, we note that the term multiplied by γ_θ drops out since the interface is assumed to be at local equilibrium. Fig. A.13 depicts a schematic illustration of Eq. (A.6), where the stiffness $\gamma_o + \gamma_{\theta\theta}$ corresponds to the local curvature of the $\Delta\gamma - \theta$ diagram. Positive (negative) stiffness values correspond to stable (unstable) configurations.

Appendix B. Expansions using Fourier series

For a function of two variables $f(x, y)$ defined over $\{-l \le x \le l, -h \le y \le h\}$, the complex form of the Fourier series expansion is [79]

$$f(x, y) = \sum_{m,n=-\infty}^{+\infty} \beta_{mn}e^{i\pi\left(\frac{m}{l}x + \frac{n}{h}y\right)}, \tag{B.1}$$

where $i = \sqrt{-1}$ and β_{mn} represent the Fourier coefficient for the (m, n) mode. The Trigonometric form of this Fourier expansion is given by [79,80]

$$f(x, y) = \sum_{m,n=0}^{\infty} \left[+ A_{mn}\cos\left(\frac{m\pi x}{l}\right)\cos\left(\frac{n\pi y}{h}\right) \right.$$
$$+ B_{mn}\sin\left(\frac{m\pi x}{l}\right)\cos\left(\frac{n\pi y}{h}\right)$$
$$+ C_{mn}\cos\left(\frac{m\pi x}{l}\right)\sin\left(\frac{n\pi y}{h}\right)$$
$$\left. + D_{mn}\sin\left(\frac{m\pi x}{l}\right)\sin\left(\frac{n\pi y}{h}\right) \right], \tag{B.2}$$

where again (m, n) are integers representing the mode. Here, we note that

$$\int_{-l}^{+l} \cos\left(\frac{m\pi x}{l}\right) \cos\left(\frac{n\pi x}{l}\right) dx = l\delta_{mn} \tag{B.3a}$$

$$\int_{-l}^{+l} \sin\left(\frac{m\pi x}{l}\right) \sin\left(\frac{n\pi x}{l}\right) dx = l\delta_{mn} \tag{B.3b}$$

$$\int_{-l}^{+l} \sin\left(\frac{m\pi x}{l}\right) \cos\left(\frac{n\pi x}{l}\right) dx = 0 \tag{B.3c}$$

where δ_{mn} is the Kronecker delta. Therefore, the coeffiicients A_{mn}, B_{mn}, C_{mn} and D_{mn} represent an orthogonal projection of $f(x, y)$ onto the basis associated with (m, n). The formal approach of fitting the GB energy functions using the spherical angles θ and ϕ is to enumerate through the (m, n) modes starting with the smallest values. However, one can identify the dominant modes by examining the symmetry in the GB energy data shown in Fig. 3.

Supplementary material

Supplementary material associated with this article can be found, in the online version, at 10.1016/j.actamat.2021.117220

References

[1] J. Crank, Free and Moving Boundary Problems, Oxford, 1984.
[2] J.S. Langer, Instabilities and pattern formation in crystal growth, Rev. Mod. Phys. 52 (1980) 1–28.
[3] A. Karma, W.J. Rappel, Quantitative phase-field modeling of dendritic growth in two and three dimensions, Phys. Rev. E 57 (1998) 4323–4349.
[4] R. Balluffi, S. Allen, W. Carter, Kinetics of Materials, Wiley, 2005.
[5] M.N. Rahaman, Ceramic Processing and Sintering, 2nd, Marcel Dekker, 2003.
[6] P.W. Voorhees, The theory of ostwald ripening, Journal of Statistical Physics 38 (1985) 231–252.
[7] D. Cogswell, Quantitative phase-field modeling of dendritic electrodeposition, Phys. Rev. E 92 (2015) 011301.
[8] M. Gurtin, Multiphase thermomechanics with interfacial structure. 1.heat–conduction and the capillary balance law, Arch. Rat. Mech. Ana. 104 (1988) 195–221.
[9] N. Provatas, K. Elder, Phase-Field Methods in Materials Science and Engineering, Wiley-VCH, 2010.
[10] F.J. Humphreys, M. Hatherly, Recrystallization and related annealing phenomena, Elsevier, 2012.
[11] L.S.G. Gottstein, Grain Boundary Migration in Metals: Thermodynamics, Kinetics, Applications, 2nd, CRC Press, 2010.
[12] A. Rollett, D. Srolovitz, M. Anderson, Simulation and theory of abnormal grain growth-anisotropic grain boundary energies and mobilities, Acta Metall. 37 (1989) 1227–1240.
[13] V. Randle, The measurement of grain boundary geometry, Taylor & Francis, 1993a.
[14] V. Randle, The measurment of grain boundary geometry, Inst. of Phys. Pub., 1993b.
[15] D. Rowenhorst, A.D. Rollett, G.S. Rohrer, M. Groeber, M. Jackson, P.J. Konijnenberg, M.D. Graef, Consistent representations of and conversions between 3d rotations, Mod. Sim. Mater. Sci. Eng. 23 (2015).
[16] D. Olmsted, S.M. Foiles, E. Holm, Survey of computed grain boundary properties in face-centered cubic metals: I. grain boundary energy, Acta Mater. 57 (2009a) 3694–3703.
[17] D. Olmsted, E. Holm, S.M. Foiles, Survey of computed grain boundary properties in face-centered cubic metals: II. grain boundary mobility, Acta Mater. 57 (2009b) 3704–3713.
[18] A. Suzuki, Y. Mishin, Atomic mechanisms of grain boundary diffusion: Low versus high temperatures, Journal of materials science 40 (2005) 3155–3161.
[19] H. Lee, M. Shabani, G.J. Pataky, F. Abdeljawad, Tensile deformation behavior of twist grain boundaries in cocrfemnni high entropy alloy bicrystals, Scientific reports 11 (2021).
[20] D.E. Spearot, M.A. Tschopp, K.I. Jacob, D.L. McDowell, Tensile strength of < 100 > and < 110 > tilt bicrystal copper interfaces, Acta materialia 55 (2007) 705–714.
[21] X.-M. Bai, L.J. Vernon, R.G. Hoagland, A.F. Voter, M. Nastasi, B.P. Uberuaga, Role of atomic structure on grain boundary-defect interactions in cu, Physical Review B 85 (2012) 214103.
[22] W. Han, M. Demkowicz, E. Fu, Y. Wang, A. Misra, Effect of grain boundary character on sink efficiency, Acta materialia 60 (2012) 6341–6351.
[23] C. Herring, Surface tension as a motivation for sintering, in: W.E. Kingston (Ed.), The physics of powder metallurgy, McGraw-Hill, NY, 1951, pp. 143–179.
[24] S. Angenent, M. Gurtin, Multiphase thermomechanics with interfacial structure. 2. evolution of an isothermal interface, Arch. Rat. Mech. Ana. 108 (1989) 323–391.
[25] M. Gurtin, A. Struthers, Multiphase thermomechanics with interfacial structure. 3. evolving phase boundaries in the presence of bulk deformation, Arch. Rat. Mech. Ana. 112 (1990) 97–160.
[26] F. Abdeljawad, D.L. Medlin, J.A. Zimmerman, K. Hattar, S.M. Foiles, A diffuse interface model of grain boundary faceting, J. App. Phys. 119 (2016) 235306.
[27] D. Du, H. Zhang, D.J. Srolovitz, Properties and determination of the interface stiffness, Acta Mater. 55 (2007) 467–471.
[28] S. Torabi, J. Lowengrub, A. Voigt, S. Wise, A new phase-field model for strongly anisotropic systems, Proc. Roy. Soc. A 465 (2009) 1337–1359.
[29] D. Medlin, K. Hattar, J. Zimmerman, F. Abdeljawad, S. Foiles, Defect character at grain boundary facet junctions: Analysis of an asymmetric $\Sigma = 5$ grain boundary in fe, Acta Mater. 124 (2017) 383–396.
[30] T. Hsieh, R. Balluffi, Observations of roughening/de-faceting phase transitions in grain boundaries, Acta Metallurgica 37 (1989) 2133–2139.
[31] S.B. Lee, D.Y. Yoon, N.M. Hwang, M.F. Henry, Grain boundary faceting and abnormal grain growth in nickel, Metallurgical and materials transactions A 31 (2000) 985–994.
[32] J.W. Cahn, Transitions and phase equilibria among grain boundary structures, J. Phys.-Paris 43 (1982) 199–213.
[33] S.M. Foiles, J. Hoyt, Computation of grain boundary stiffness and mobility from boundary fluctuations, Acta Mater. 54 (2006) 3351–3357.
[34] H. Zhang, D. Du, D.J. Srolovitz, M.I. Mendelev, Determination of grain boundary stiffness from molecular dynamics simulation, App. Phys. Lett. 88 (2006) 121927.
[35] A.A. Schratt, I. Steinbach, V. Mohles, Grain boundary energy landscape from the shape analysis of synthetically stabilized embedded grains, Computational Materials Science 193 (2021) 110384.
[36] F. Abdeljawad, S.M. Foiles, A.P. Moore, A.R. Hinkle, C.M. Barr, N.M. Heckman, K. Hattar, B.L. Boyce, The role of the interface stiffness tensor on grain boundary dynamics, Acta Materialia 158 (2018) 440–453.
[37] N. Cabrera, The equilibrium of crystal surfaces, Surf. Sci. 2 (1964) 320–345.
[38] V. Privman, Fluctuating interfaces, surface tension, and capillary waves: An introduction, Int. J. Mod. Phys. C 03 (1992) 857–877.
[39] M. Gurtin, Toward a nonequilibrium thermodynamics of 2-phase materials, Arch. Rat. Mech. Ana. 100 (1988) 275–312.
[40] J.-M. Debierre, A. Karma, F. Celestini, R. Guérin, Phase-field approach for faceted solidification, Phys. Rev. E 68 (2003) 041604.
[41] G. Wulff, Xxv. zur frage der geschwindigkeit des wachsthums und der auflösung der krystallflächen, Zeitschrift für Kristallographie-Crystalline Materials 34 (1901) 449–530.
[42] F.C. Frank, The geometrical thermodynamics of surfaces, in: Metal surfaces: Structure, energetics and kinetics, Amer. Soc. Metals, Metal Park, OH, 1963, pp. 1–15.
[43] C. Herring, Some theorems on the free energies of crystal surfaces, Phys. Rev. 82 (1951) 87–93.
[44] D. Hoffman, J.W. Cahn, A vector thermodynamics for anisotropic surfaces i. fundamentals and application to plane surface junctions, Surf. Sci. 31 (1972) 368–388.
[45] J.W. Cahn, D. Hoffman, A vector thermodynamics for anisotropic surfaces II. curved and faceted surfaces, Acta Metall. 22 (1974) 1205–1214.
[46] R.F. Sekerka, Analytical criteria for missing orientations on three-dimensional equilibrium shapes, Journal of crystal growth 275 (2005) 77–82.
[47] A. Di Carlo, M. Gurtin, P. Podio-Guidugli, A regularized equation for anisotropic motion-by-curvature, SIAM J. Appl. Math. 52 (1992) 1111–1119.
[48] A. Wheeler, Cahn-hoffman ξ-vector and its relation to diffuse interface models of phase transitions, J. Stat. Phys. 95 (1999) 1245–1280.
[49] A. Wheeler, Phase-field theory of edges in an anisotropic crystal, Proc. Roy. Soc. A 462 (2006) 3363–3384.
[50] W.W. Mullins, Theory of linear facet growth during thermal etching, Philos. Mag. A 6 (1961) 1313–1341.
[51] W.W. Mullins, Solid surface morphologies governed by capillarity, in: Metal surfaces: Structure, energetics and kinetics, Amer. Soc. Metals, Metal Park, OH, 1963, pp. 17–66.
[52] J. Stewart, N. Goldenfeld, Spinodal decomposition of a crystal surface, Phys. Rev. A 46 (1992) 6505–6512.
[53] S. Wise, J. Lowengrub, J. Kim, K. Thornton, P.W. Voorhees, W. Johnson, Quantum dot formation on a strain-patterned epitaxial thin film, App. Phys. Lett. 87 (2005) 133102.
[54] J. Eggleston, G. McFadden, P. Voorhees, A phase-field model for highly anisotropic interfacial energy, Physica D 150 (2001) 91–103.
[55] J. Eggleston, P. Voorhees, Ordered growth of nanocrystals via a morphological instability, App. Phys. Lett. 80 (2002).
[56] W.W. Mullins, Two-dimensional motion of idealized grain boundaries, J. App. Phys. 27 (1956) 900–904.
[57] J. Burke, D. Turnbull, Recrystallization and grain growth, Prog. Metal. Phys. 3 (1952) 220–292.
[58] J.J. Hoyt, M. Asta, A. Karma, Method for computing the anisotropy of the solid-liquid interfacial free energy, Phys. Rev. Lett. 86 (2001) 5530–5533.
[59] X. Zhong, M.N. Kelly, H.M. Miller, S.J. Dillon, G.S. Rohrer, Grain boundary curvatures in polycrystalline srtio3: Dependence on grain size, topology, and crystallography, Journal of the American Ceramic Society 102 (2019) 7003–7014.
[60] J.E. Taylor, li'mean curvature and weighted mean curvature, Acta metallurgica et materialia 40 (1992) 1475–1485.

[61] G.S. Rohrer, E.A. Holm, A.D. Rollett, S.M. Foiles, J. Li, D.L. Olmsted, Comparing calculated and measured grain boundary energies in nickel, Acta Materialia 58 (2010) 5063–5069.

[62] A.P. Sutton, R.W. Balluffi, Interfaces in Crystalline Materials, Clarendon Press, 2003.

[63] S. Patala, C.A. Schuh, Symmetries in the representation of grain boundary–plane distributions, Philosophical Magazine 93 (2013) 524–573.

[64] E.R. Homer, S. Patala, J.L. Priedeman, Grain boundary plane orientation fundamental zones and structure-property relationships, Sci. Reports 5 (2015).

[65] E. Miyoshi, T. Takaki, Validation of a novel higher-order multi-phase-field model for grain-growth simulations using anisotropic grain-boundary properties, Computational Materials Science 112 (2016) 44–51.

[66] V. Tikare, E. Holm, D. Fan, L.Q. Chen, Comparison of phase-field and potts models for coarsening processes, Acta materialia 47 (1998) 363–371.

[67] E.A. Lazar, J.K. Mason, R.D. MacPherson, D.J. Srolovitz, A more accurate three--dimensional grain growth algorithm, Acta Materialia 59 (2011) 6837–6847.

[68] M. Upmanyu, G.N. Hassold, A. Kazaryan, E.A. Holm, Y. Wang, B. Patton, D.J. Srolovitz, Boundary mobility and energy anisotropy effects on microstructural evolution during grain growth, Interface Science 10 (2002) 201–216.

[69] V. Randle, G. Rohrer, H. Miller, M. Coleman, G. Owen, Five-parameter grain boundary distribution of commercially grain boundary engineered nickel and copper, Acta materialia 56 (2008) 2363–2373.

[70] G.S. Rohrer, The grain boundary data archive, 2018, http://mimp.materials.cmu.edu/~gr20/Grain_Boundary_Data_Archive/.

[71] D.M. Saylor, B.S. El-Dasher, B.L. Adams, G.S. Rohrer, Measuring the five-parameter grain-boundary distribution from observations of planar sections, Metallurgical and Materials Transactions A 35 (2004) 1981–1989.

[72] E.A. Holm, D.L. Olmsted, S.M. Foiles, Comparing grain boundary energies in face-centered cubic metals: Al, au, cu and ni, Scripta Materialia 63 (2010) 905–908.

[73] MathWorks, Matlab r2019a, 2021, URL https://www.mathworks.com/products/new_products/release2019a.html.

[74] Wolfram, Mathematica v11, 2021,URL https://www.wolfram.com/mathematica/new-in-11/.

[75] K. Miyazawa, Y. Iwasaki, K. Ito, Y. Ishida, Combination rule of σ values at triple junctions in cubic polycrystals, Acta Crystallographica Section A: Foundations of Crystallography 52 (1996) 787–796.

[76] B. Straumal, S. Polyakov, E. Mittemeijer, Temperature influence on the faceting of $\sigma 3$ and $\sigma 9$ grain boundaries in cu, Acta materialia 54 (2006) 167–172.

[77] A. Kazaryan, Y. Wang, S. Dregia, B.R. Patton, Generalized phase-field model for computer simulation of grain growth in anisotropic systems, Physical Review B 61 (2000) 14275.

[78] W. Yang, L.-Q. Chen, G.L. Messing, Computer simulation of anisotropic grain growth, Materials Science and Engineering: A 195 (1995) 179–187.

[79] A.D. Poularikas, Handbook of formulas and tables for signal processing, CRC press, 2018.

[80] M.A. Pinsky, Introduction to Fourier analysis and wavelets, 102, American Mathematical Society, 2008.